PHYSICAL REVIEW B **109**, 075132 (2024)

Dual-polarization helical interface states in inverse-designed photonic crystals with glide symmetry

Yafeng Chen,[1] Hai-Xiao Wang,[2,*] Zhihao Lan,[3] and Zhongqing Su[1,†]

[1]*Department of Mechanical Engineering, The Hong Kong Polytechnic University, Hong Kong SAR, People's Republic of China*
[2]*School of Physical Science and Technology, Ningbo University, Ningbo 315211, China*
[3]*Department of Electronic and Electrical Engineering, University College London, London WC1E 7JE, United Kingdom*

(Received 14 September 2023; revised 22 November 2023; accepted 23 January 2024; published 14 February 2024)

Photonic analogs of topological crystalline insulators (PTCIs) that host pseudospin-locked unidirectional helical interface states have promising applications for developing novel integrated optical devices. However, current PTCIs are limited to a single polarization. Here, we propose a dual-polarization PTCI hosting topological interface states for both transverse electric (TE) and transverse magnetic (TM) modes. First, we design a photonic crystal (PC), constrained with glide symmetry, with a dual-polarization bulk gap via inverse design. Then, by adopting two kinds of unit cells with different topology indexes from the PC and arranging them to form an interface, pseudospin-locked unidirectional helical interface states are observed. Pseudospin-locked one-way propagations of edge states for both TE and TM modes are demonstrated. Besides the polarization-independent function, we also present the polarization-dependent propagation of interface states by tuning the frequency. Our work demonstrates the flexible manipulation of light in PTCIs with the polarization degree of freedom, having promising applications in developing both polarization-independent and polarization-dependent topological optical devices.

DOI: 10.1103/PhysRevB.109.075132

I. INTRODUCTION

The discovery of photonic topological insulators (PTIs) has revolutionized the way of light manipulation and opened doors for developing photonic devices [1–10]. Inspired by the topological band theory in condensed matter physics, various photonic analogs of topological insulators have been proposed to mimic different topological phases in electronic systems. The first version of PTIs featured with unidirectional and backscattering immune electromagnetic waves was achieved using a gyromagnetic photonic crystals (PCs) platform, which mimics the famous quantum Hall effect [11–13]. However, the requirement of the breaking of time-reversal symmetry makes them incompatible with integrated optical devices. To overcome it, photonic analogs of topological crystalline insulators (PTCIs) [14–17], which take full advantage of the crystalline symmetry and hence go beyond the material limitation, have been proposed. For instance, by breaking the spatial inversion or mirror symmetry of triangular or honeycomb PCs, one may achieve the PTCI with valley kink states [18–21]. Another common PTCI is the so-called bosonic Z_2 topological crystalline insulator with robust pseudospin dependent edge states, which was proposed by Wu *et al.* in expanded and shrunken honeycomb lattice [14–17]. Besides, nonsymmorphic symmetry, e.g., glide and screw symmetry, which consists of mirror/rotation symmetry and a translation operation, has proven to be a powerful tool to realize PTCIs with pseudospin dependent edge states [22–25]. Moreover, by further considering the topology of the edge states, higher-order PTIs going beyond the conventional bulk-boundary correspondence have also been proposed [26–35].

It is worth noting that most studies of all-dielectric PTIs are realized in two-dimensional systems since the electromagnetic wave can be decoupled into two orthogonal polarization modes, that is, the transverse electric (TE) mode with in-plane electric fields, and the transverse magnetic (TM) mode with in-plane magnetic fields [36], making it more accessible than that in three dimensions. On the other hand, the dual-polarization photonic devices, including dual-polarization interferometry [37], dual-polarization laser [38], dual-polarization nonlinear enhancement [39,40], dual-polarization photonic integrated circuits [41], and dual-polarization beam splitter [42], have attracted significant attention since they can be further multiplexed to enlarge the optical information-processing capacity of integrated optical devices. Hence, it is highly desirable to realize the dual-polarization PTCIs from an application perspective. Very recently, dual-polarizations PTCIs with valley kink states have been proposed [43–45].

In this work, we design a dual-polarization PTCI supporting pseudospin-locked unidirectional helical electromagnetic waves with both TM and TE modes at the same interface. A PC constrained with glide and mirror symmetries is first designed to have a dual-polarization bulk gap via inverse design. By adopting two kinds of unit cells with different topological crystalline indexes and arranging them to form an interface, pseudospin-locked unidirectional helical interface states are observed. The polarization-independent high-efficiency

---

[*] wanghaixiao@nbu.edu.cn
[†] zhongqing.su@polyu.edu.hk

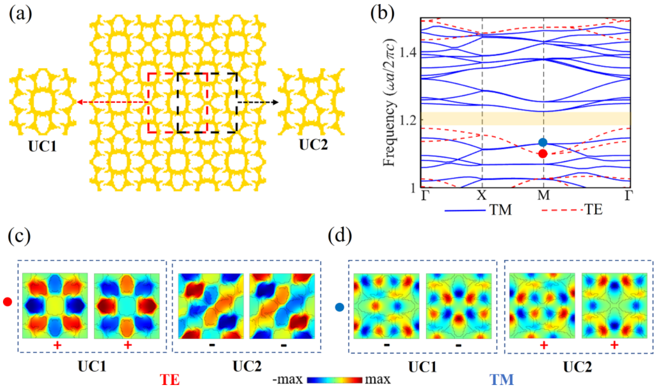

FIG. 1. (a) The optimized PC. (b) The band diagram of the optimized PC. (c), (d) Eigenmodes at the M point of the bands below the complete band gap for UC1 and UC2 for TE and TM modes.

propagation and pseudospin-locked unidirectional transmission of interface states are demonstrated. In addition to the polarization-independent function, we also present the polarization-dependent propagation of interface states by modulating the frequency. Our work suggests a route for developing both polarization-independent and polarization-dependent topological optical devices.

II. RESULTS AND DISCUSSION

To design the dual-polarization PTCI, we first constraint the PC with glide and mirror symmetries [46], which plays a key role in realizing topological crystalline insulators in classical wave systems, and then utilize the inverse design method to open a complete band gap for both TM and TE modes, as introduced in Appendix A. Throughout this work, the angular frequency ω is normalized as $\Omega = \omega a/2\pi c$, where a and c denote the lattice constant and light speed, respectively. For simplicity, the PC is made of dielectric materials with a relative permittivity of 12, and the complete band gap is opened by maximizing the minimum imaginary part of wave vectors for both TM and TE modes at normalized frequency $\Omega = 1.2$. Figures 1(a) and 1(b) show the optimized PC and its band diagram, within which the blue solid line and pink dashed line represent TM and TE modes, respectively. Remarkably, all bands appear in pairs along the Brillouin zone boundary line MX due to the introduction of the glide symmetry (see Appendix B for details), which plays a key role on the emergence of the helical interface states. It is also observed that there is a complete band gap (denoted by the yellow area) ranging $\Omega = 1.150 - 1.217$ for both TE and TM modes. The band gap for the TE mode locates between the 14th band and the 15th band, whereas it locates between the 24th band and the 25th band for the TM mode.

Next, we adopt two primitive cells from the optimized PC: the UC1 (denoted by the pink box) and the UC2 (denoted by the black box) obtained by translating the UC1 along the horizontal direction with $a/2$. Because UC1 and UC2 are adopted from the same PC, they share the same band diagram. However, the eigenmodes at high symmetry points of each band can be different. As shown in Figs. 1(c) and 1(d), we present the eigenmodes at the M point (labeled by the colorful circles) of the bands below the complete band gap for UC1 and UC2 for the TE and TM modes, respectively. It can be seen that, for the TE mode, the first two modes below the gap are of even parities for UC1 and are of odd parities for UC2. In contrast, for the TM mode, the first two modes below the gap are of odd parities for UC1 and are of even parities for UC2. Actually, regardless of the polarization, the parities of the eigenmodes of a specific band at M are opposite for UC1 and UC2. Hence, a parity-inversion band gap forms when UC1 and UC2 are placed together, which results in the emergence of interface states within the complete band gap according to the Jackiw-Rebbi theory [47].

Moreover, we use the symmetry indicators to characterize the bulk topology of UC1 and UC2. The PTCI in this work exhibits with both C_2 and time-reversal symmetries, hence, according to Refs. [48,49], the topological crystalline index can be expressed as $\chi = ([X_1], [Y_1], [M_1])$, where $[\Pi_1] = \#\Pi_1 - \#\Gamma_1 (\Pi = X, Y, M)$, and $\#\Pi_1^{(2)} (\#\Gamma_1^{(2)})$ denotes the number of bands below the band gap with even parity eigenvalues of C_2 symmetry at the Π and Γ points for all bands below the band gap [50]. Accordingly, for the TE mode, $\chi = (0, 0, 0)$ for UC1 and $\chi = (-2, -2, -2)$ for UC2; for the TM mode, $\chi = (0, 0, -2)$ for UC1 and $\chi = (0, 0, 2)$ for UC2. It is worth noting that the trivial atomic insulators (namely, the band gap formed by uncoupled atoms) have $[\Pi_1] = 0$ for all the high symmetry points, while any nonzero $[\Pi_1]$ indicates a topological band gap that is adiabatically disconnected from the trivial atomic insulator. Hence, for the TE modes, while UC1 is topologically trivial, UC2 is topological nontrivial. Differently, for the TM modes, both UC1 and UC2 are topologically nontrivial. Nonetheless, the topology crystalline indexes of UC1 and UC2 for both TE and TM modes are different, predicting the emergence of interface states at the domain wall between UC1 and UC2 for both TE and TM modes [48,49]. It is also worth noting that not all UCs selected from the optimized PCs via the inverse design method have distinct topological crystalline indexes, and therefore we conduct several optimizations and choose the PC with the desired topological indexes as shown in Fig. 1(a).

To verify our predictions, we study the domain wall systems formed by the UC1 and UC2 for both TE and TM polarizations. Owing to the lack of C_{4v} symmetry, the vertical and horizontal interfaces formed by UC1 and UC2 are not equivalent. Therefore, we construct two supercells with vertical and horizontal interfaces formed by UC1 and UC2, respectively (see the schematic in Appendix C), which are termed as SCV and SCH, respectively. For the vertical interfaces, the projected band diagrams for TE and TM modes are shown in Figs. 2(a) and 2(b), respectively, where the gray regions and lines represent the projections of bulk bands and the dispersions of edge states. As expected, both diagrams indicate that interface states within the bulk gap emerge at the domain walls. For the TE modes, the frequency window of the interface states is (1.154, 1.407), while for the TM modes, there are two pairs of interface states, of which the frequency windows are (1.14, 1.149) and (1.163, 1.216), respectively, separated by a gap emerging in the bulk band gap. Since the parity-inversion picture is valid as long as the supercell contains both UC1 and UC2, the interface states within the lower frequency window can be regarded as a physical manifestation

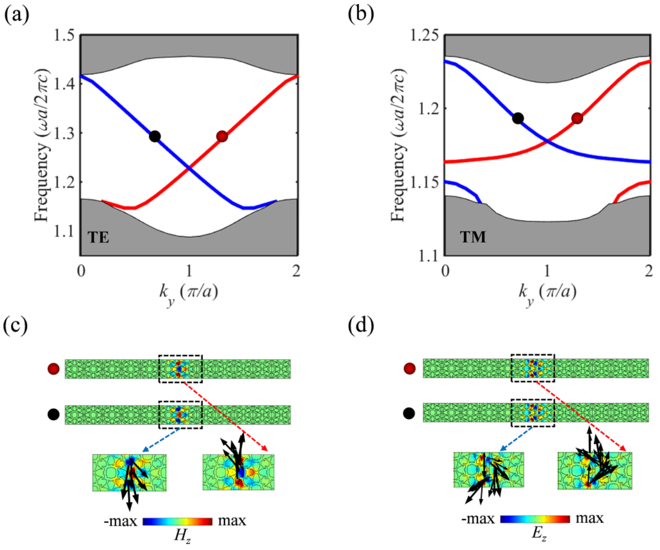

FIG. 2. Interface states of the vertical interfaces. (a),(b) Projected band diagrams of SCV for TE and TM modes, respectively. (c), (d) The eigenfields at $k_y = 0.7\pi/a$ (black balls) and $k_y = 1.3\pi/a$ (red balls) for TE and TM modes, respectively. The enlarged views of black dashed boxes show the energy flux distributions.

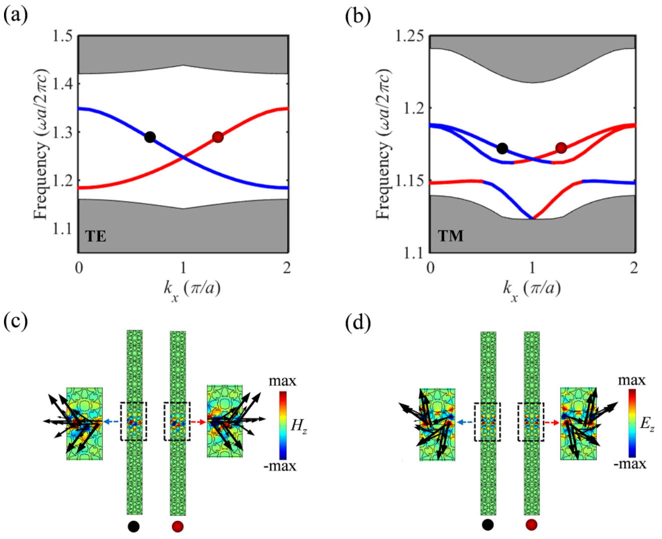

FIG. 3. Interface states of the horizontal interfaces. (a),(b) Projected band diagrams of SCH for TE and TM modes, respectively. (c), (d) The eigenfields at $k_x = 0.7\pi/a$ (blue balls) and $k_x = 1.3\pi/a$ (red balls) for TE and TM modes, respectively. The enlarged views of black dashed boxes show the energy flux distributions.

of the parity inversion of the lower bulk band. It is also seen that one edge band indicated by a red line has a positive group velocity whereas the other edge band indicated by a blue line has a negative group velocity, which are intersected at $k_y = \pi/a$. The degeneracy of the helical interface states at $k_y = \pi/a$ results from the combination of the space group symmetry of the waveguide and its periodicity along the glide dislocation [51]. Figures 2(c) and 2(d) display the two typical eigenfields of the interface states and their Poynting vector distributions at $k_y = 0.7\pi/a$ (black balls) and $k_y = 1.3\pi/a$ (red balls) for TE and TM modes, respectively. The Poynting vector distributions (also see the enlarged views of black dashed boxes) show that the interface states with $k_y = 0.7\pi/a$ and $k_y = 1.3\pi/a$ of the same frequency exhibit opposite energy flows, unveiling the intriguing spin-momentum locking feature of the helical interface states.

For the horizontal interfaces, we display the projected band diagrams for TE and TM modes in Figs. 3(a) and 3(b), respectively. It is seen that a pair of interface states for the TE mode, of which the frequency window is (1.173, 1.339), emerge within the bulk gap. Meanwhile, for the TM mode, two pairs of interface states originated from parity inversion of lower bands experience a band anticrossing around $k_x = 0.5\pi/a$, resulting in two frequency windows, namely, (1.14, 1.149) and (1.161, 1.187). We also plot the eigenfields and energy flux distributions at $k_x = 0.7\pi/a$ (blue balls) and $k_x = 1.3\pi/a$ (red balls) for TE and TM modes in Figs. 3(c) and 3(d), respectively, showing that energies are highly localized at the interface between UC1 and UC2 and the energy of interface states denoted by red and blue balls flows rightward and leftward, respectively, indicating the interface states of TM mode also carry finite orbital angular momentum (OAM).

Considering the frequency windows of the interface states for TE and TM modes, the overlapped frequency windows of the interface states between TE and TM modes are (1.163,1.216) and (1.173,1.187) for SCV and SCH, respectively, within which the dual-polarization interface states can survive. Figures 4(a) and 4(d) display the transmission spectra of electromagnetic waves propagating along the vertical and horizontal channels formed by UC1 and UC2 (as sketched in Appendix D), respectively, where the bulk gap is within the black dashed lines and the blue (yellow) area refers to the overlapped frequency windows of dual-polarization interface states supported by the vertical (horizontal) channel. It is seen that within the overlapped frequency windows, the dual-polarization interface states propagating along the vertical and horizontal channels exhibit high transmission ratios for both TE and TM waves. Figures 4(b) [4(e)] and 4(c) [4(f)] give absolute electric and magnetic field distributions at $\Omega = 1.18$ of TE- and TM-polarized waves propagating along vertical (horizontal) channels, from which we can observe high-efficiency transmission of both TE- and TM-polarized waves propagating along the vertical and horizontal channels. Therefore, dual-polarization interface states with the same frequency propagating along the edge channel are realized.

Furthermore, we demonstrate pseudospin-momentum locking for dual-polarization interface states along the vertical channel. To excite pseudospin-momentum-locked interface states, we use a four-antenna array at the center of the vertical channel to generate electromagnetic waves carrying positive OAM (counterclockwise rotating energy flow) and negative OAM (clockwise rotating energy flow). Figure 5 shows the pseudospin-locked one-way propagation for TE- and TM-polarized waves at $\Omega = 1.203$, wherein we can observe upward unidirectional propagation of TE- and TM-polarized waves carrying positive OAM [see Figs. 5(a) and 5(c)] and downward unidirectional propagation of TE- and TM-polarized waves carrying negative OAM [see Figs. 5(b) and 5(d)]. Therefore, pseudospin-locked one-way propagation of dual-polarization interface states is achieved.

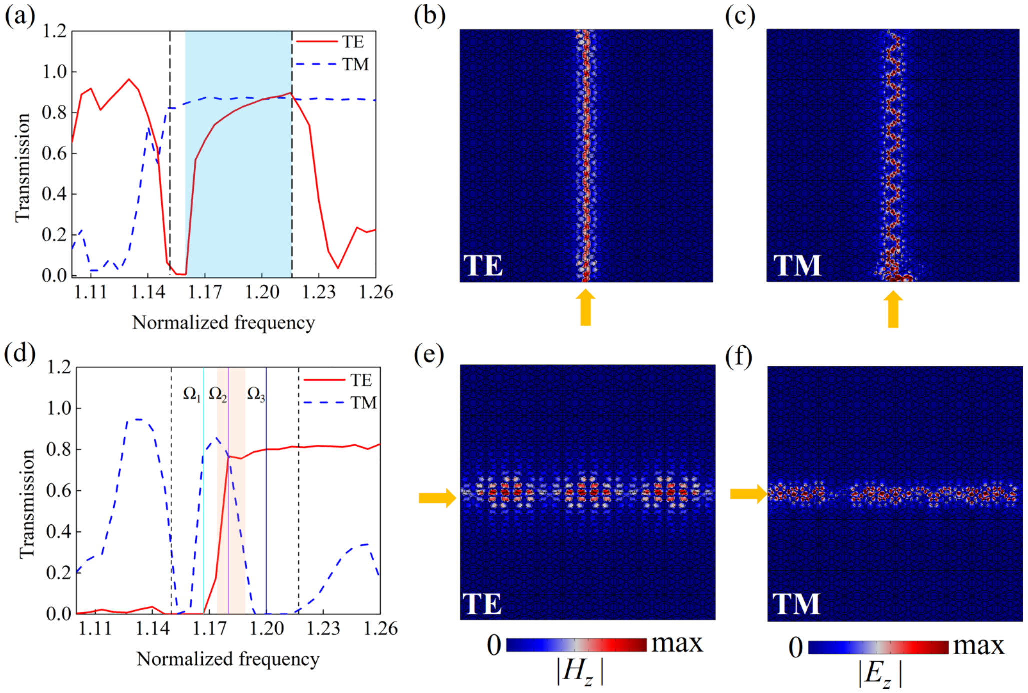

FIG. 4. (a), (d) Transmission spectra of electromagnetic waves propagating along the (a) vertical and (d) horizontal channels. (b), (c) Absolute field distributions at $\Omega = 1.18$ of (b) TE- and (c) TM-polarized waves propagating along the vertical channel. (e), (f) Absolute field distributions at $\Omega = 1.18$ of (e) TE- and (f) TM-polarized waves propagating along the horizontal channel.

The mismatch of the frequency window of interface states for TE and TM modes may find potential application in a photonic beam splitter. As depicted in Fig. 6, a horizontal channel formed by UC1 and UC2 is designed as a polarization-dependent beam splitter. When an excitation source, with frequency $\Omega_1 = 1.167$ [see the green line in Fig. 4(d)], is excited, it is expected that only TM-polarized waves can pass through the horizontal channel while TE-polarized waves cannot [see Figs. 6(a) and 6(d)]. Increasing the frequency of the excitation source to $\Omega_2 = 1.18$ [see the purple line in Fig. 4(d)], both TE- and TM-polarized waves can pass through the channel [see Figs. 6(b) and 6(e)]. Further increasing the frequency of the excitation source to $\Omega_3 = 1.2$ [see the black line in Fig. 4(d)] results in the propagation of TE-polarized waves and the forbidden propagation of the TM-polarized waves [see Figs. 6(c) and 6(f)]. Therefore, the frequency can be used to turn on or off the propagation of TE- and TM-polarized waves along the interface.

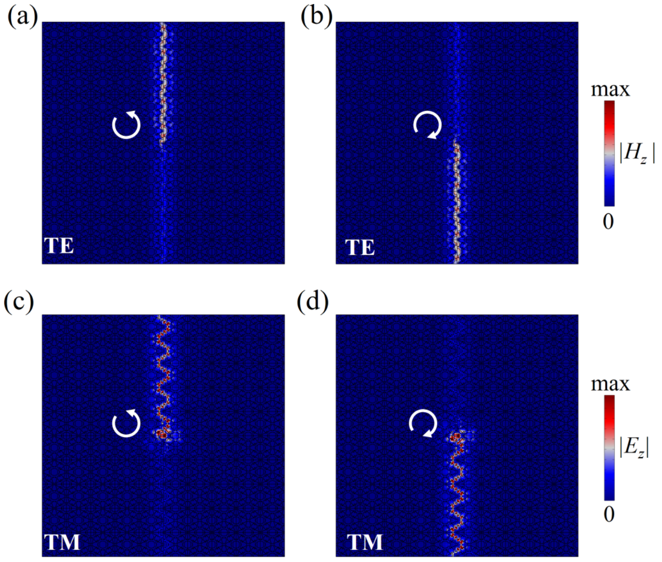

FIG. 5. Pseudospin-locked one-way propagation of dual-polarization interface states. (a), (b) Upward and downward unidirectional propagation of TE-polarized waves carrying positive and negative OAM. (c),(d) Upward and downward unidirectional propagation of TM-polarized waves carrying positive and negative OAM.

III. CONCLUSIONS

To conclude, we propose a dual-polarization PTCI in all-dielectric PCs with glide symmetry. Pseudospin-locked helical interface states are achieved for both TE and TM modes. The high-efficiency transmission and pseudospin-locked one-way propagation of interface states for both TE and TM polarizations are realized. In this way, two different optical signals can be separately encoded into TE- and TM-polarized waves so that the optical information processing capacity of the dual-polarization PTCI can be doubled. Besides, we present the polarization-dependent propagation of interface states by modulating the frequency, that is, the channels for TE- and TM-polarized waves can be separately turned on or off, which can be exploited for developing topologically protected polarization multiplexing devices. Furthermore, the dual-polarization PTCI has promising applications in the development of dual-polarization topological interferometry,

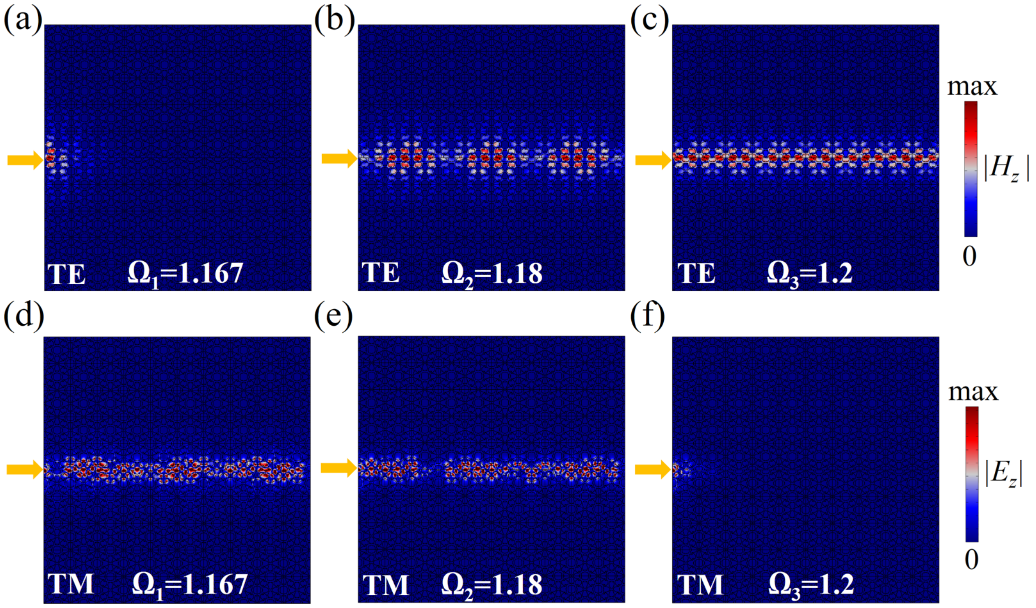

FIG. 6. (a)–(c) Absolute magnetic field distributions of TE-polarized waves propagating along the horizontal channel at (a) $\Omega_1 = 1.167$, (b) $\Omega_2 = 1.18$, and (c) $\Omega_3 = 1.2$, respectively. (d)–(f) Absolute electric field distributions of TM-polarized waves propagating along the horizontal channel at (d) $\Omega_1 = 1.167$, (e) $\Omega_2 = 1.18$, and (f) $\Omega_3 = 1.2$, respectively.

dual-polarization topological lasers, dual-polarization topological nonlinear enhancement devices, and dual-polarization topological photonic integrated circuits. Finally, we would like to mention that advanced fabrication techniques, such as 3D printing technology in microwave regime [52] and electron beam lithography technology [53–56] at optical wavelengths, are readily available to fabricate complicated PC structures designed via the inverse design method. Moreover, the fine details of the optimized PC structures typically have size of $a/10$, which only affect physics above frequencies of $\sim 10c/a$, a scale much larger than the operational frequencies of the helical interface states at around $\sim c/a$ (see, e.g., Figs. 2 and 3).

ACKNOWLEDGMENTS

This work was supported by National Natural Science Foundation of China (Grants No. 12102134 and No. 11904060), the Natural Science Foundation of Hunan Province (Grant No. 2022JJ40026), and the Research Grants Council of Hong Kong SAR (Grants No. 15200922, No. 15205219, No. 15202820, and No. 15204419).

APPENDIX A: INVERSE DESIGN METHOD TO OPEN A COMPLETE BAND GAP

The eigenvalue equations of 2D PCs for the TM and TE modes can be expressed as [36,57]

$$(\nabla + i\mathbf{k}) \cdot [(\nabla + i\mathbf{k})E(\mathbf{r})] = \varepsilon(\mathbf{r})\left(\frac{\omega}{c}\right)^2 E(\mathbf{r}) \text{ for TM}, \tag{A1a}$$

$$-(\nabla + i\mathbf{k}) \cdot \left(\frac{1}{\varepsilon(\mathbf{r})}(\nabla + i\mathbf{k})H(\mathbf{r})\right) = \left(\frac{\omega}{c}\right)^2 H(\mathbf{r}) \text{ for TE}, \tag{A1b}$$

in which $\varepsilon(\mathbf{r})$, $E(\mathbf{r})$, and $H(\mathbf{r})$ represent the dielectric constant, the electric field, and the magnetic field at position $\mathbf{r}$, respectively; $\mathbf{k} = (k_x, k_y)$ is the Bloch wave vector. Because Eqs. (A1) have two unknown variables $\mathbf{k}$ and ω, two methods, the $\omega(\mathbf{k})$ method based on classical band theory and the $\mathbf{k}(\omega)$ method based on complex band theory, can be adopted to solve it. Here, we adopt the $\mathbf{k}(\omega)$ method and k_x and k_y are set as $k_x = k\cos\theta$ and $k_y = k\sin\theta$, respectively, where θ denotes the wave vector direction. Using the finite element method, Eqs. (A1) can be formulated as the following matrix form:

$$(k^2\mathbf{K_I} + k\mathbf{K_{II}} + \mathbf{K_{III}})\mathbf{u} = \mathbf{0}, \tag{A2}$$

where $\mathbf{u}$ denotes the eigenvector of the electric or magnetic field. The detailed expressions of matrix K_{I}, K_{II}, and K_{III} for TM and TE modes can be found in Ref. [57]. Then, the quadratic eigenvalue equation Eq. (A2) can be converted into the standard eigenvalue problem as

$$[\mathbf{K}(\theta, \omega) - k\mathbf{M}(\theta)]\bar{\mathbf{U}} = \mathbf{0}, \tag{A3}$$

where $\mathbf{K} = \begin{bmatrix} \mathbf{K_{II}} & \mathbf{K_{III}} \\ \mathbf{I} & \mathbf{0} \end{bmatrix}$, $\mathbf{M} = \begin{bmatrix} -\mathbf{K_I} & \mathbf{0} \\ \mathbf{0} & \mathbf{I} \end{bmatrix}$, $\bar{\mathbf{U}} = \begin{bmatrix} k\mathbf{u} \\ \mathbf{u} \end{bmatrix}$. After solving Eq. (A3) at the specific ω and θ, we can get k in a complex form, $k' + ik''$. Previous work indicates that the complete band gap can be automatically opened by maximizing the minimum k'' of all wave vector directions at the given frequency for both TM and TE modes. For the PC with glide symmetry, $\theta \in [0, \frac{\pi}{4}]$. Therefore, the inverse design formulation can be expressed by

$$\begin{aligned} \max:\quad & f(x_e) = \min(k''_{\theta_g,\mathrm{TM}}, k''_{\theta_g,\mathrm{TE}}) \\ \text{s.t.}:\quad & \theta_g \in \left[0 : \frac{\pi}{36} : \frac{\pi}{4}\right] \\ & x_e = 0 \text{ or } 1;\ e = 1,\ 2, \cdots,\ m, \end{aligned} \tag{A4}$$

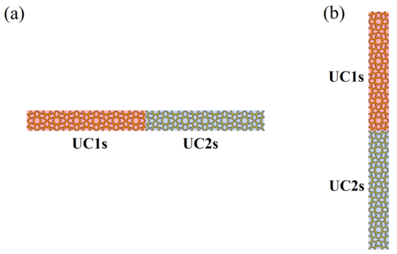

FIG. 7. Schematics of (a) SCV and (b) SCH.

where the unit cell is discretized as m elements and x_e denotes the design variable of the element e, which equals 1 when the element is full of silicon, whereas it is 0 for air. $k''_{\theta_g,\mathrm{TM}}$ and $k''_{\theta_g,\mathrm{TE}}$ denote the minimum imaginary part of the wave vector at the specific direction θ_g for TM and TE modes, respectively. To update the design variables, the sensitivity of each element should be derived, which can be calculated upon getting $\frac{k''_{\theta_g,\mathrm{TM}}}{\partial x_e}$ and $\frac{k''_{\theta_g,\mathrm{TE}}}{\partial x_e}$. Differentiating both sides of Eq. (A2), we can get

$$\frac{\partial k''_{\theta_g,\mathrm{TM/TE}}}{\partial x_e} = imag\left(-\frac{\mathbf{v}^T\left(k^2_{\theta_g,\mathrm{TM/TE}}\frac{\partial \mathbf{K_I}}{\partial x_e}+k_{\theta_g,\mathrm{TM/TE}}\frac{\partial \mathbf{K_{II}}}{\partial x_e}+\frac{\partial \mathbf{K_{III}}}{\partial x_e}\right)\mathbf{u}}{2k_{\theta_g,\mathrm{TM/TE}}\mathbf{v}^T\,\mathbf{K_I}\mathbf{u}+\mathbf{v}^T\,\mathbf{K_{II}}\mathbf{u}}\right). \tag{A5}$$

Upon getting sensitivities of all elements, we use the gradient-based optimization algorithm to iteratively update the design variables until the optimal structure is obtained [57].

APPENDIX B: BAND DEGENERACY ALONG HIGH SYMMETRY LINE *XM*

Note that all bands appear in pairs along the Brillouin zone boundary line MX, which can be understood as the result of the glide symmetries $G_x : (x, y) \rightarrow (x + \frac{a}{2}, \frac{a}{2} - y)$.

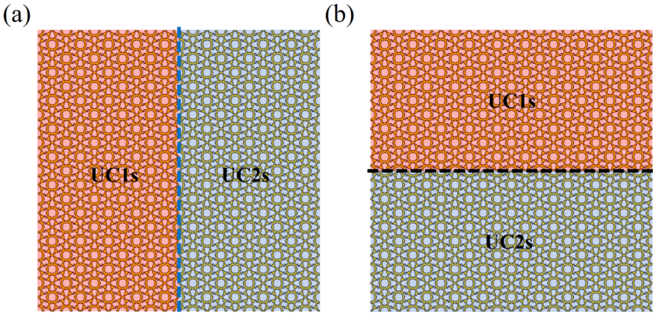

FIG. 8. Sketch of the channels formed by UC1s and UC2s. (a) The vertical channel. (b) The horizontal channel.

When combined with the time-reversal operation T, the antiunitary symmetry operators $\Theta_x = G_x * T$ enable the double degeneracy at the Brillouin zone boundary. For example, $\Theta_x^2\Psi_{n,\mathbf{k}} = e^{ik_xa}\Psi_{n,\mathbf{k}}$, where $\Psi_{n,\mathbf{k}}$ is a Bloch wave function for the electromagnetic field, and n and $\mathbf{k}$ are the band index and wave vector, respectively. Hence, at the Brillouin zone boundary line MX, namely, $k_xa = \pi$, we have $\Theta_x^2 = -1$, inducing fermioniclike Kramers double degeneracy.

APPENDIX C: SCHEMATICS OF SUPERCELLS FOR CALCULATING INTERFACE STATES

Figures 7(a) and 7(b) show the schematics of supercells, made of six UC1s and UC2s, for calculating interface states along the vertical interface and the horizontal interface, which are named SCV and SCH, respectively.

APPENDIX D: SKETCH OF VERTICAL AND HORIZONTAL CHANNELS FORMED BETWEEN UC1s AND UC2s

Figures 8(a) and 8(b) show the sketch of the vertical and horizontal channels formed by UC1s and UC2s, respectively; they are labeled by the blue dashed line and the black dashed line, respectively.

---

[1] L. Lu, J. D. Joannopoulos, and M. Soljačić, Topological photonics, Nat. Photon. **8**, 821 (2014).

[2] A. B. Khanikaev and G. Shvets, Two-dimensional topological photonics, Nat. Photon. **11**, 763 (2017).

[3] T. Ozawa, H. M. Price, A. Amo, N. Goldman, M. Hafezi, L. Lu, M. C. Rechtsman, D. Schuster, J. Simon, O. Zilberberg, and I. Carusotto, Topological photonics, Rev. Mod. Phys. **91**, 015006 (2019).

[4] M. Kim, Z. Jacob, and J. Rho, Recent advances in 2D, 3D and higher-order topological photonics, Light: Sci. Appl. **9**, 130 (2020).

[5] H.-X. Wang and Jian-Hua Jiang, A short review of all-dielectric topological photonic crystals, Front. Phys. **10**, 17 (2022).

[6] C. Guo, V. S. Asadchy, B. Zhao, and S. J. e. Fan, Light control with weyl semimetals, Elight **3**, 2 (2023).

[7] Z. Chen and M. Segev, Highlighting photonics: looking into the next decade, Elight **1**, 2 (2021).

[8] Y. Zhang, D. Bongiovanni, Z. Wang, X. Wang, S. Xia, Z. Hu, D. Song, D. Jukić, J. Xu, and R. J. e. Morandotti, Realization of photonic p-orbital higher-order topological insulators, Elight **3**, 5 (2023).

[9] Z. Lan, Y. Chen, L. An, and Z. Su, Chern, dipole, and quadrupole topological phases of a simple magneto-optical photonic crystal with a square lattice and an unconventional unit cell, Phys. Rev. B **109**, 045402 (2024).

[10] Z. Lan, Y. Chen, J. Zhu, and Z. J. O. L. Su, Quadrupole topological phases and filling anomaly in all-dielectric Lieb lattice photonic crystals, Opt. Lett. **48**, 5747 (2023).

[11] F. D. M. Haldane and S. Raghu, Possible realization of directional optical waveguides in photonic crystals with broken time-reversal symmetry, Phys. Rev. Lett. **100**, 013904 (2008).

[12] Z. Wang, Y. D. Chong, J. D. Joannopoulos, and M. Soljačić, Reflection-free one-way edge modes in a gyromagnetic photonic crystal, Phys. Rev. Lett. **100**, 013905 (2008).

[13] Z. Wang, Y. Chong, J. D. Joannopoulos, and M. Soljačić, Observation of unidirectional backscattering-immune topological electromagnetic states, Nature (London) **461**, 772 (2009).

[14] L.-H. Wu and X. Hu, Scheme for achieving a topological photonic crystal by using dielectric material, Phys. Rev. Lett. **114**, 223901 (2015).

[15] L. Xu, H.-X. Wang, Y.-D. Xu, H.-Y. Chen, and J.-H. Jiang, Accidental degeneracy in photonic bands and topological phase transitions in two-dimensional core-shell dielectric photonic crystals, Opt. Express **24**, 18059 (2016).

[16] Y. Yang, Y. F. Xu, T. Xu, H.-X. Wang, J.-H. Jiang, X. Hu, and Z. H. Hang, Visualization of a unidirectional electromagnetic waveguide using topological photonic crystals made of dielectric materials, Phys. Rev. Lett. **120**, 217401 (2018).

[17] Y. Chen, F. Meng, B. Jia, G. Li, and X. Huang, Inverse design of photonic topological insulators with extra-wide bandgaps, Phys. Status Solidi RRL **13**, 1900175 (2019).

[18] X.-T. He, E.-T. Liang, J.-J. Yuan, H.-Y. Qiu, X.-D. Chen, F.-L. Zhao, and J.-W. Dong, A silicon-on-insulator slab for topological valley transport, Nat. Commun. **10**, 872 (2019).

[19] J.-W. Liu, F.-L. Shi, X.-T. He, G.-J. Tang, W.-J. Chen, X.-D. Chen, and J.-W. Dong, Valley photonic crystals, Adv. Phys. X **6**, 1905546 (2021).

[20] H. Xue, Y. Yang, and B. Zhang, Topological valley photonics: physics and device applications, Adv. Photonics Res. **2**, 2100013 (2021).

[21] S. Shao, L. Liang, J.-H. Hu, Y. Poo, and H.-X. Wang, Topological edge and corner states in honeycomb-kagome photonic crystals, Opt. Express **31**, 17695 (2023).

[22] H.-X. Wang, Y. Chen, Z. H. Hang, H.-Y. Kee, and J.-H. Jiang, Type-II dirac photons, npj Quantum Mater. **2**, 54 (2017).

[23] X. Zhang, H.-X. Wang, Z.-K. Lin, Y. Tian, B. Xie, M.-H. Lu, Y.-F. Chen, and J.-H. Jiang, Second-order topology and multidimensional topological transitions in sonic crystals, Nat. Phys. **15**, 582 (2019).

[24] L. Zhang, Y. Yang, Z. Lin, P. Qin, Q. Chen, F. Gao, E. Li, J. Jiang, B. Zhang, and H. Chen, Higher-order topological states in surface-wave photonic crystals, Adv. Sci. **7**, 1902724 (2020).

[25] H.-X. Wang, Y. Chen, G.-Y. Guo, H.-Y. Kee, and J.-H. Jiang, Possible realization of optical dirac points in woodpile photonic crystals, Opt. Express **30**, 17204 (2022).

[26] B. Xie, H.-X. Wang, X. Zhang, P. Zhan, J.-H. Jiang, M. Lu, and Y. Chen, Higher-order band topology, Nat. Rev. Phys. **3**, 520 (2021).

[27] B. Xie, G. Su, H.-F. Wang, F. Liu, L. Hu, S.-Y. Yu, P. Zhan, M.-H. Lu, Z. Wang, and Y.-F. Chen, Higher-order quantum spin hall effect in a photonic crystal, Nat. Commun. **11**, 3768 (2020).

[28] B.-Y. Xie, H.-F. Wang, H.-X. Wang, X.-Y. Zhu, J.-H. Jiang, M.-H. Lu, and Y.-F. Chen, Second-order photonic topological insulator with corner states, Phys. Rev. B **98**, 205147 (2018).

[29] B.-Y. Xie, G.-X. Su, H.-F. Wang, H. Su, X.-P. Shen, P. Zhan, M.-H. Lu, Z.-L. Wang, and Y.-F. Chen, Visualization of higher-order topological insulating phases in two-dimensional dielectric photonic crystals, Phys. Rev. Lett. **122**, 233903 (2019).

[30] X.-D. Chen, W.-M. Deng, F.-L. Shi, F.-L. Zhao, M. Chen, and J.-W. Dong, Direct observation of corner states in second-order topological photonic crystal slabs, Phys. Rev. Lett. **122**, 233902 (2019).

[31] Y. Chen, F. Meng, Z. Lan, B. Jia, and X. Huang, Dual-polarization second-order photonic topological insulators, Phys. Rev. Appl. **15**, 034053 (2021).

[32] Y. Chen, F. Meng, Y. Kivshar, B. Jia, and X. Huang, Inverse design of higher-order photonic topological insulators, Phys. Rev. Res. **2**, 023115 (2020).

[33] Y. Chen, Z. Lan, and J. Zhu, Inversely designed second-order photonic topological insulator with multiband corner states, Phys. Rev. Appl. **17**, 054003 (2022).

[34] Y. Chen, Z. Lan, and J. Zhu, Second-order topological phases in C_{4v}-Symmetric photonic crystals beyond the two-dimensional Su-Schrieffer–Heeger model, Nanophotonics **11**, 1345 (2022).

[35] Y. Chen, Z. Lan, J. Li, and J. Zhu, Topologically protected second harmonic generation via doubly resonant high-order photonic modes, Phys. Rev. B **104**, 155421 (2021).

[36] J. D. Joannopoulos, S. G. Johnson, J. N. Winn, and R. D. Meade, *Photonic Crystals: Molding the Flow of Light*, 2nd ed. (Princeton University Press, Princeton, 2008).

[37] J. Escorihuela, M. Á. González-Martínez, J. L. López-Paz, R. Puchades, Á. Maquieira, and D. Gimenez-Romero, Dual-polarization interferometry: a novel technique to light up the nanomolecular world, Chem. Rev. **115**, 265 (2015).

[38] J. Thévenin, M. Vallet, and M. Brunel, Dual-polarization mode-locked ND:YAG laser, Opt. Lett. **37**, 2859 (2012).

[39] M. Minkov, D. Gerace, and S. Fan, Doubly resonant $\chi^{(2)}$ nonlinear photonic crystal cavity based on a bound state in the continuum, Optica **6**, 1039 (2019).

[40] D. Smirnova, D. Leykam, Y. Chong, and Y. Kivshar, Nonlinear topological photonics, Appl. Phys. Rev. **7**, 021306 (2020).

[41] D. Dai, L. Liu, S. Gao, D.-X. Xu, and S. He, Polarization management for silicon photonic integrated circuits: polarization management for silicon photonic integrated circuits, Laser Photonics Rev. **7**, 303 (2013).

[42] X.-T. He, C.-H. Guo, G.-J. Tang, M.-Y. Li, X.-D. Chen, and J.-W. Dong, Topological polarization beam splitter in dual-polarization all-dielectric valley photonic crystals, Phys. Rev. Appl. **18**, 044080 (2022).

[43] L. He, H. Zhang, W. Zhang, Y. Wang, and X. Zhang, Topologically protected vector edge states and polarization beam splitter by all-dielectric valley photonic crystal slabs, New J. Phys. **23**, 093026 (2021).

[44] X.-T. He, J.-W. Liu, F.-L. Shi, K. Shen, W.-J. Chen, X.-D. Chen, and J.-W. Dong, Dual-polarization two-dimensional valley photonic crystals, Sci. China: Phys., Mech. Astron. **65**, 284212 (2022).

[45] J. Hu, Y. Wang, J. Niu, C. Wang, T. Liu, L. Shi, Y. Zhang, Y. Xia, and K. Chang, Observation of dual-polarization topological photonic states at optical frequencies, Laser Photonics Rev. **17**, 2300515 (2023).

[46] Z.-K. Lin, H.-X. Wang, Z. Xiong, M.-H. Lu, and J.-H. Jiang, Anomalous quadrupole topological insulators in two-dimensional nonsymmorphic sonic crystals, Phys. Rev. B **102**, 035105 (2020).

[47] R. Jackiw and C. Rebbi, Solitons with fermion number $^{1}/_{2}$, Phys. Rev. D **13**, 3398 (1976).

[48] S. Vaidya, A. Ghorashi, T. Christensen, M. C. Rechtsman, and W. A. Benalcazar, Topological phases of photonic crystals under crystalline symmetries, Phys. Rev. B **108**, 085116 (2023).

[49] W. A. Benalcazar, T. Li, and T. L. Hughes, Quantization of fractional corner charge in C_n-Symmetric higher-order topological crystalline insulators, Phys. Rev. B **99**, 245151 (2019).

[50] Y. Wu, M. Yan, Z.-K. Lin, H.-X. Wang, F. Li, and J.-H. Jiang, On-chip higher-order topological micromechanical metamaterials, Sci. Bull. **66**, 1959 (2021).

[51] J. A. Iglesias Martínez, N. Laforge, M. Kadic, and V. Laude, Topological waves guided by a glide-reflection symmetric crystal interface, Phys. Rev. B **106**, 064304 (2022).

[52] N. M. Estakhri, B. Edwards, and N. Engheta, Inverse-designed metastructuresthat solve equations, Science **363**, 1333 (2019).

[53] A. Y. Piggott, J. Lu, K. G. Lagoudakis, J. Petykiewicz, T. M. Babinec, and J. Vučković, Inverse design and demonstration of a compact and broadband on-chip wavelength demultiplexer, Nat. Photonics **9**, 374 (2015).

[54] K. Y. Yang, J. Skarda, M. Cotrufo, A. Dutt, G. H. Ahn, M. Sawaby, D. Vercruysse, A. Arbabian, S. Fan, A. Alù, and J. Vučković, Inverse-designed non-reciprocal pulse router for chip-based LiDAR, Nat. Photon. **14**, 369 (2020).

[55] K. Y. Yang, C. Shirpurkar, A. D. White, J. Zang, L. Chang, F. Ashtiani, M. A. Guidry, D. M. Lukin, S. V. Pericherla, J. Yang, H. Kwon, J. Lu, G. H. Ahn, K. Van Gasse, Y. Jin, S.-P. Yu, T. C. Briles, J. R. Stone, D. R. Carlson, H. Song *et al.*, Multidimensional data transmission using inverse-designed silicon photonics and microcombs, Nat. Commun. **13**, 7862 (2022).

[56] R. J. Gelly, A. D. White, G. Scuri, X. Liao, G. H. Ahn, B. Deng, K. Watanabe, T. Taniguchi, J. Vučković, and H. Park, An inverse-designed nanophotonic interface for excitons in atomically thin materials, Nano Lett. **23**, 8779 (2023).

[57] Y. Chen, F. Meng, G. Li, and X. Huang, Designing photonic materials with complete band gaps by topology optimization, Smart Mater. Struct. **28**, 015025 (2019).